Chapter 6
Dynamics

Ayano Chiba and Shinya Hosokawa

Abstract In this chapter, we review the wavenumber and energy ranges covered by various dynamics measurement methods and then outline inelastic neutron scattering (INS) and inelastic X-ray scattering (IXS) in particular. We explain their principles and methods and pick up recent applications and developments. As an example of recent INS research, a study of a solid refrigerant is first introduced, since Å-level dynamics contributes to thermal properties. For another example, we look at recent advances on the boson peak, which is an excitation that is universally seen in structurally disordered systems. As an example of recent IXS studies, we pick up the measurement of phonon dispersion relations of Mg alloys, which are expected to be the next-generation structural material. In the last part of this chapter, we introduce recently developed measurement techniques of IXS in which Mössbauer nuclei are excited by synchrotron radiation and used for dynamic measurements.

Keywords Inelastic neutron scattering · Inelastic X-ray scattering · Relaxation · Phonon · Magnon

6.1 Introduction

Hyperordered structures are difficult to understand by ordinary diffraction experiments alone. By combining dynamic measurements with static measurements such as diffraction, it is possible to understand the structures both in space and time axes. Since dynamic measurements often do not require atomic periodicity, they will have great potential in investigating typical hyperordered structures in functional

A. Chiba (✉)
Department of Physics, Keio University, Yokohama 223-8522, Japan
e-mail: ayano@phys.keio.ac.jp

S. Hosokawa
Institute of Industrial Nanomaterials, Kumamoto University, Kumamoto 860-8555, Japan
e-mail: shhosokawa@kumamoto-u.ac.jp

materials, such as formations of clusters, the co-doping of impurity elements, or element-vacancy correlations.

In Sect. 6.2, we will look at several dynamical methods for investigating different space and time scales. Some traditional macro-, meso-, and microscopic methods are introduced by applying different external fields to target materials, such as optic, electric, magnetic, and acoustic fields. In Sect. 6.3, we explain how inelastic scattering experiments can provide the dynamic structure of materials. In Sects. 6.4–6.7, we describe inelastic scattering measurements using neutron and synchrotron radiation quantum beams, describing their advantages and disadvantages, giving examples of experimental results, and introducing new measurement methods that have recently been developed. Finally, overall features of dynamical methods for investigating hyperordered structures of materials are summarized in Sect. 6.8.

6.2   Space and Time Scales of Dynamical Methods

Movements of atoms have various scales in space length (or wavenumber) and time (or frequency). Figure 6.1 shows the wavenumber (space)–energy (time) scales accessible by various measurement techniques, frequently employed in studies such as Ref. [1]. The corresponding correlation length r and the atomic/molecular motion time t are also indicated at the top- and right-hand side of the figure. To investigate the dynamics of materials, it is important to choose an appropriate method for the length and time scales of interest, as well as to know the advantages and disadvantages of experimental methods. In this section, we focus on the measurements of atomic-scale microscopic dynamics using quantum beams and present typical examples of hyperordered structure measurement.

Thus far, optical methods have frequently been used for investigating the dynamics of materials, particularly localized vibration modes. Some examples are Raman scattering, infrared (IR) absorption spectroscopy, and Brillouin scattering, which are shown in Fig. 6.1, depending on the excitation energies of interest. Since the energy of light is low for visible and infrared light, the observable Q ranges are very limited, as shown in the figure. Photon correlation spectroscopy (PCS) can reach very low energies. The recently developed X-ray photon correlation spectroscopy (XPCS) technique widely expands the observable Q range up to several 10 nm^{-1} with a very low excitation energy. Inelastic ultraviolet scattering (IUVS) is also a relatively new dynamics measurement technique that emerged in the 2000s and has a wavenumber range lower than that of neutrons and an energy range by which one can measure the speed of sound in some materials. Neutron spin echo (NSE) is a well-established technique that covers the lowest energy region in neutron-based dynamics measurements.

Since this book mainly covers structures on space scales of around Å order, here we focus on methods that enable the simultaneous measurement of the time axis and the space axis of Å order, namely, we focus on inelastic neutron scattering (INS, Sect. 6.4) and inelastic X-ray scattering (IXS, Sect. 6.5). We would also like to briefly
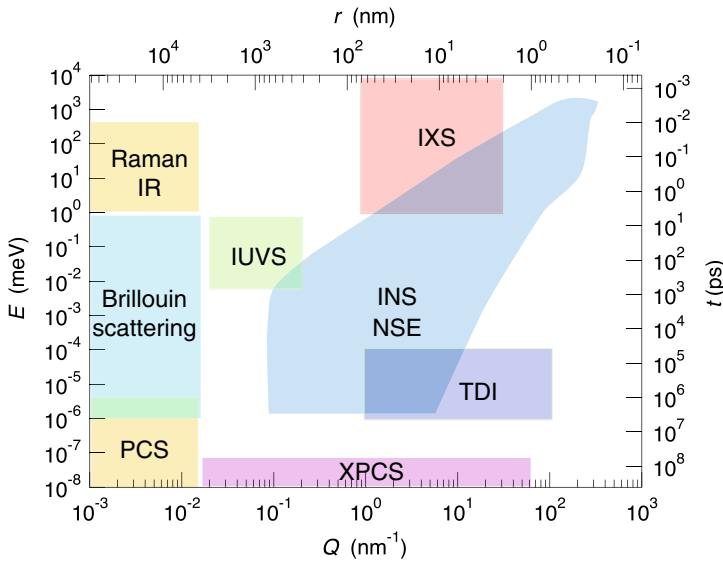
Fig. 6.1 Wide ranges of wavenumber Q–energy E space and areas accessible by several experimental techniques. See texts for details. The corresponding correlation time t and length r are also indicated at the right and top axes, respectively

Fig. 6.2 Schematic diagram of inelastic scattering
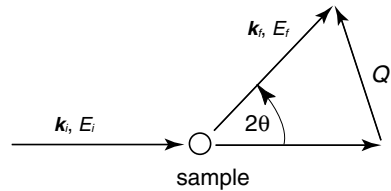
introduce two recently developed methods that use the Mössbauer effect excited by synchrotron radiation: nuclear resonant inelastic X-ray scattering (NRIXS, Sect. 6.6), by which one can selectively measure the dynamics of atoms that have Mössbauer nuclei, and time-domain interferometry (TDI, Sect. 6.7), by which one can measure the region around 10 nm^{-1}, 10 neV, which was not covered previously.

6.3 Principles of Inelastic Scattering

Figure 6.2 shows a typical inelastic scattering experiment. Suppose an incident neutron or X-ray beam with wave vector k_i and energy E_i. A scattered beam changes both the wave vector and energy to k_f and E_f, respectively. Then, the scattering intensity $S(Q, E)$ can be described as a function of wave vector transfer, $Q = k_f - k_i$, and energy transfer, $E = E_f - E_i$. $S(Q, E)$ is referred to as the dynamic structure factor.

$S(\mathbf{Q}, E)$ can be separated into two factors as

$$S(\mathbf{Q}, E) = S_{\mathrm{inc}}(\mathbf{Q}, E) + S_{\mathrm{coh}}(\mathbf{Q}, E),$$

where $S_{\mathrm{inc}}(\mathbf{Q}, E)$ and $S_{\mathrm{coh}}(\mathbf{Q}, E)$ represent incoherent and coherent dynamic structure factors, respectively, denoting the self- and pair parts of this function.

To discuss the physical meaning of the $S(\mathbf{Q}, E)$ function, we should start with the Van Hove space-time correlation function [2],

$$G(\mathbf{r}, t) = \frac{1}{N} \langle n(\mathbf{0}, 0)n(\mathbf{r}, t) \rangle,$$

where

$$n(\mathbf{r}, t) = \sum_{j=1}^{N} \delta(\mathbf{r} - \mathbf{r}_j(t))$$

is the number density as functions of $\mathbf{r}$ and t, and $\langle \rangle$ represents the average over the system. The $G(\mathbf{r}, t)$ function is also separated into the self- and pair correlation functions ($G_{\mathrm{s}}(\mathbf{r}, t)$ and $G_{\mathrm{p}}(\mathbf{r}, t)$, respectively) as

$$G(\mathbf{r}, t) = G_{\mathrm{s}}(\mathbf{r}, t) + G_{\mathrm{p}}(\mathbf{r}, t).$$

Here, $G_{\mathrm{s}}(\mathbf{r}, t)$ is the probability of finding a particle at position $\mathbf{r}$ and time t if *the same particle* was at position $\mathbf{0}$ and time 0. On the other hand, $G_{\mathrm{p}}(\mathbf{r}, t)$ is that if *any particle* was at position $\mathbf{0}$ and time 0.

The intermediate scattering function $I(\mathbf{Q}, t)$ introduced by Van Hove [2] can be written as

$$I(\mathbf{Q}, t) = \frac{1}{N} \sum_{i=1}^{N} \sum_{j=1}^{N} \langle \exp[-i\mathbf{Q} \cdot \mathbf{r}_i(0)] \exp[+i\mathbf{Q} \cdot \mathbf{r}_j(t)] \rangle$$

$$= \frac{1}{N} \sum_{i=1}^{N} \sum_{j=1}^{N} \langle \exp[-i\mathbf{Q} \cdot \{\mathbf{r}_i(0) - \mathbf{r}_j(t)\}] \rangle.$$

Note that the self-part of $I(\mathbf{Q}, t)$, $I_{\mathrm{s}}(\mathbf{Q}, t)$, means $i = j$, i.e.,

$$I_{\mathrm{s}}(\mathbf{Q}, t) = \frac{1}{N} \sum_{j=1}^{N} \langle \exp[-i\mathbf{Q} \cdot \{\mathbf{r}_j(0) - \mathbf{r}_j(t)\}] \rangle,$$

and the pair part $I_{\mathrm{p}}(\mathbf{Q}, t)$ is the remainder.

This function is also connected with a space-Fourier transform of $G(\mathbf{r}, t)$, i.e.,

$$I(\boldsymbol{Q}, t) = \int_V G(\boldsymbol{r}, t) \exp(i\boldsymbol{Q} \cdot \boldsymbol{r}) \mathrm{d}\boldsymbol{r}, \tag{6.1}$$

and the $S(\boldsymbol{Q}, E)$ function is a time-Fourier transform of $I(\boldsymbol{Q}, t)$, i.e.,

$$S(\boldsymbol{Q}, E) = \frac{1}{2\pi} \int_{-\infty}^{\infty} I(\boldsymbol{Q}, t) \exp(-iEt/\hbar) \mathrm{d}t.$$

As indicated by these equations, the information directly obtained from scattering experiments is the Fourier transform of real space and time. For static structures, the fact that the scattering amplitude is given by the three-dimensional Fourier transform of the real-space potential (first-order Born approximation) is explained as a consequence of simple scattering theory in Ref. [3].

Note that in the above equation, $S_{\mathrm{inc}}(\boldsymbol{Q}, E)$ and $S_{\mathrm{coh}}(\boldsymbol{Q}, E)$ can be calculated from $I_{\mathrm{s}}(\boldsymbol{Q}, t)$ and $I_{\mathrm{p}}(\boldsymbol{Q}, t)$, respectively. Therefore, $G(\boldsymbol{r}, t)$ can, in principle, be evaluated from the space–time double Fourier transforms of the experimentally obtained $S(\boldsymbol{Q}, E)$ function. Because of the limited space and time ranges in the experimental data, however, it is not easy to obtain $G(\boldsymbol{r}, t)$ without special analytical elaborations.

The spatial range of primary interest in the structure of hyperordered materials is on the order of Å. Since neutrons have mass whereas X-rays have no mass, the energy E of wavelength $\lambda = 1$ Å, for example, can be estimated as

$$
\begin{aligned}
\text{(Neutron)} \quad & E = P^2/2m_{\mathrm{n}} \sim 81.8 \text{ meV}, \\
\text{(X-ray)} \quad & E = hc/\lambda \quad\ \sim 12.4 \text{ keV},
\end{aligned}
$$

where P and m_{n} are the momentum and the mass of the neutron, respectively, h is Planck's constant, and c is the speed of light. Compared with these is the energy we aim to measure, e.g., phonons, on the meV order. To measure such dynamics, scattered waves in which meV-order excitations are added to or subtracted from the incident energy must be resolved from the incident wave. Therefore, INS historically had an advantage in studying phonons, because IXS requires a precise energy resolution of at least $\Delta E/E_i \sim 10^{-7}$ for the incident energy E_i. In other words, a very sharp monochromatic technique is required. Nowadays, the achievable resolutions of INS and IXS are on the order of 1 μeV and 1 meV, respectively, and thus dynamics are actively measured by both techniques.

6.4 Inelastic Neutron Scattering (INS)

Historically, neutron scattering had been the only available technique for measuring collective dynamics, including phonons and slow dynamics, such as diffusion, because it requires a resolution of at least the meV order. For example, a Nobel Prize

winner, B. N. Brockhouse, measured INS on liquid water to investigate its diffusive motion in 1959 [4].

Although it is now possible to measure dynamics with X-rays, neutron scattering has the following four advantages: First, high-energy-resolution measurement is possible. An energy resolution up to three orders of magnitude higher than that of X-rays can be achieved. For example, for quasi-elastic scattering instruments, a near-backscattering spectrometer DNA at J-PARC, Japan, has a standard resolution of 2–20 μeV [5], whereas the best IXS resolutions are barely beginning to fall below meV.

Second, magnetic excitations can be observed in $Q-E$ space [6]. To study magnetic excitations in a wide $Q-E$ space, INS is almost the only technique available. Even with the availability of highly brilliant synchrotron radiation X-rays, there is still difficulty in completing the study of magnetic *static* structures by RIXS alone, and, moreover, since inelastic scattering is roughly more than three orders of magnitude weaker than elastic scattering in intensity, INS is likely to continue to be the main method for observing magnetic excitations.

Third, coherent and incoherent-scattering cross sections are adjustable by isotopes. By isotopic substitution, one can experimentally pick up dynamics of interest. To investigate self-diffusion, for example, it is advantageous to select nuclides with large incoherent-scattering cross sections. A list of scattering cross sections for each element and isotope, as well as abundance or half-life in nature for each nuclide, can be found in Refs. [7, 8]. With the right combination of nuclides, the diffusion of a particular element in a multi-elemental material can be measured. This technique is often used to study the diffusion of hydrogen in hydrogen storage materials.

Fourth, neutron scattering is also suitable for measuring the dynamics of light elements such as hydrogen, because the incoherent neutron-scattering cross section of hydrogen is as large as 80 barn. Elements with small atomic numbers are difficult to see using X-rays, but the order in which they are visible by neutrons varies from nuclides to nuclides, so isotope substitution can be used to adjust the visibility of certain elements.

The disadvantages of neutron scattering include the following: First, samples generally need to be mm to cm in size. The reasons for this are the small scattering probability due to fm-sized nuclei, the limited intensity of the incident neutron beam, and the difficulty in focusing neutrons. Second, some elements with high neutron absorption coefficients, such as ^{3}He, ^{6}Li, B, Gd, Cd, Au, and Hg, are difficult to measure. In practice, modern spallation neutron sources provide intense beams, so even in the presence of some of these elements static structures are becoming measurable, but the dynamics would still be difficult to observe. Third, since some elements have large incoherent-scattering lengths compared with coherent ones, such as H, ^{7}Li, and V, only self-diffusive motions can be observed for these elements, and collective information such as phonon dispersions would be difficult to measure. Fourth, the velocity of neutrons at wavelengths of about Å is slow, about several thousand m/s (about 2200 m/s for 25 meV), which limits the $Q-E$ region that can be measured. Let us look at this point in more detail below.

(a)

(b)
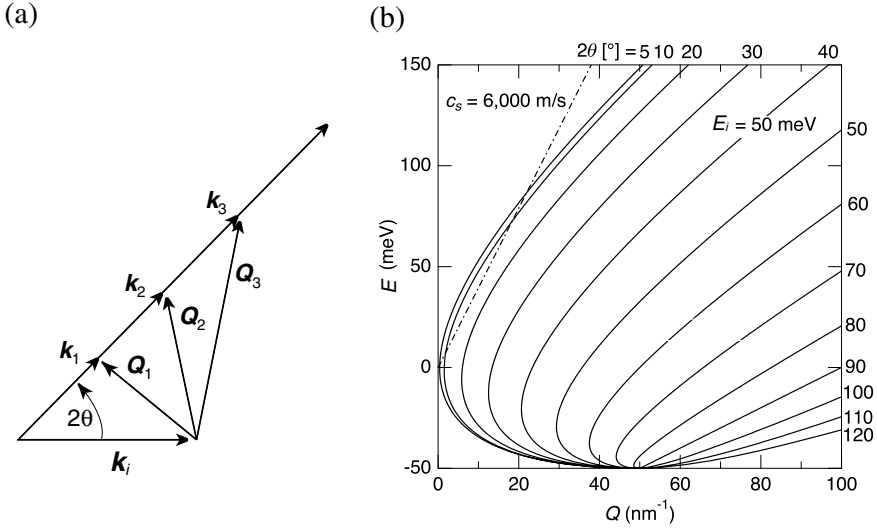
Fig. 6.3 **a** Schematic diagram of INS, and **b** typical Q–E space of INS with $E_i = 50$ meV

We briefly explain the Q–E constraint on the INS technique. A schematic diagram of inelastic scattering with $E_i =$ constant is shown in Fig. 6.3. E_is on the order of 10 meV is often used, and the magnitude of k_f changes from that of k_i, as shown in Fig. 6.3a. Thus, the magnitude of Q changes with not only the usual 2θ but also E, as expressed by

$$Q^2 = k_i^2 + k_f^2 - 2k_i k_f \cos 2\theta$$
$$= \frac{2m}{\hbar^2} \left[2E_i + E - 2\sqrt{E_i(E_i + E)} \cos 2\theta \right]. \tag{6.2}$$

Figure 6.3b shows a typical Q–E space of INS with $E_i = 50$ meV at several 2θ values. As seen in the figure, Q–E relations at constant 2θ are not straight lines but curved. Note that INS can be performed within the range of these curves. The chain line indicates the dispersion relation of longitudinal acoustic (LA) sound excitations at a low Q with a velocity of 6,000 m/s; the detailed information on this excitation cannot be evaluated by using this INS spectrometer.

For information on theoretical aspects of neutron scattering, see Ref. [9]. For information on quasi-elastic scattering in particular, see Ref. [10].

Let us look at AMATERAS, Fig. 6.4, as an example of an INS (and also quasi-elastic neutron scattering, QENS) instrument whose main research targets are phonon and magnon dispersion relations, as well as diffusion, in the energy region below 3–80 meV, depending on E_i. It can achieve a resolution of $\sim$10 μeV order if the incident energy is on the order of 1 meV [11, 12]. The instrument is characterized not only by its high resolution, but also by its high neutron intensity. To achieve high intensity,

Fig. 6.4 Schematic of
cold-neutron disk chopper
spectrometer AMATERAS
[12]
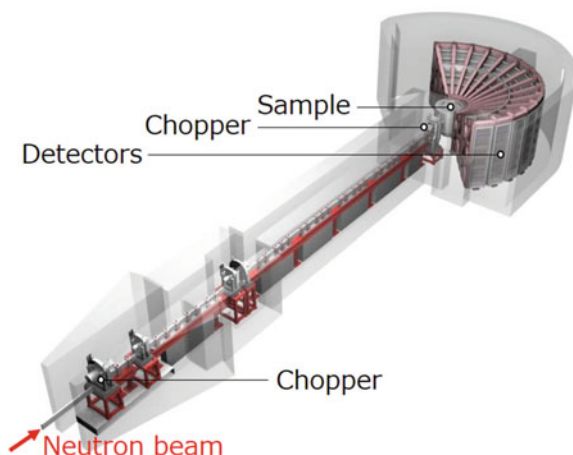
a coupled H_2 moderator is used for a source. Also, to achieve high resolution, in
addition to a disk chopper for beam monochromatization near the sample, another
chopper for pulse shaping is placed near the beam source. As a result, high-intensity
peaks are cut out with high resolution.

AMATERAS has recently been used to microscopically understand a potential
new cooling technology. In general, heat properties in solid materials are due to
the dynamics of electrons and atoms, so it is plausible that dynamics measurements
play an active role in thermal materials research. The background of this research is
that nearly 30% of all electricity is used for cooling these days, and solid refriger-
ants are attracting attention to reduce environmental impact. It has been known that
"orientation-disordered crystals", such as neopentylglycol (NPG), have a pressure-
induced calorific effect 10 times greater than that of conventional solid refrigerants,
but the microscopic mechanism had been unknown. Using AMATERAS with an
incident energy of $E_i = 2.64$ meV, Li et al. found that the free rotation motion of
NPG molecules begins in the temperature range of 300–320 K, as shown in Fig. 6.5
[13, 14]. The system changes from a monoclinic to a face-centered cubic lattice with
increasing temperature in this temperature range, as has been known from X-ray
diffraction. However, since it is the dynamics of the atoms that absorb/desorb the
heat, ordinary diffraction alone may not be able to reveal its nature as a refrigerant.
Combining these quasi-elastic neutron scattering results with molecular dynamics
simulations, it was found that the entropy change caused by the phase transition from
a state in which only the rotational relaxation of the methyl group is observed (up to
300 K) to a state in which the entire molecule can rotate (above 320 K) is respon-
sible for the solid-state caloric and "barocaloric" effects. This study is an example
of how the high energy resolution of neutron scattering can be used to understand
thermophysical properties that are directly related to atomic dynamics.

For structurally disordered systems, some progress achieved using INS instru-
ments, including AMATERAS, has recently been reported in the study of the "boson
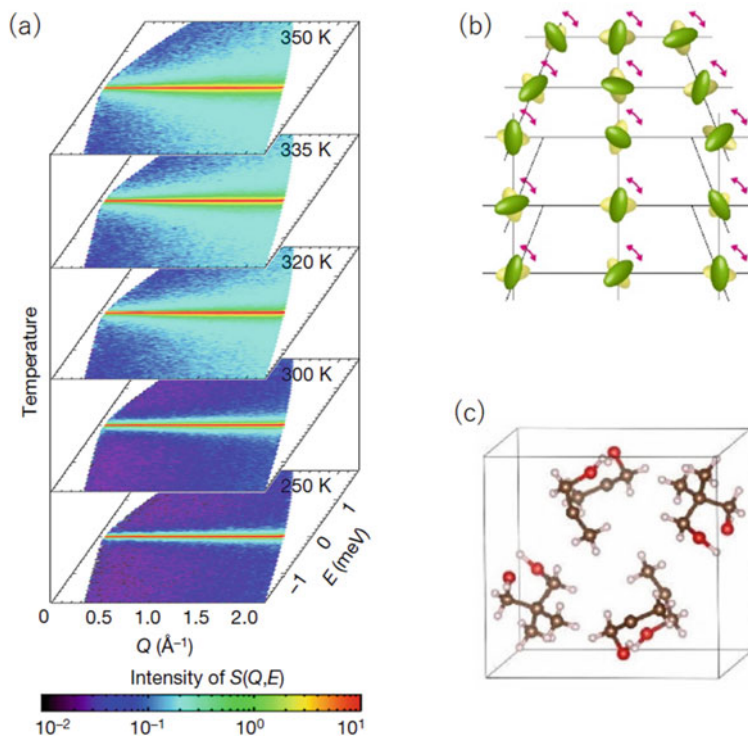
Fig. 6.5 Observed dynamics and its schematic picture of neopentylglycol (NPG) molecules [13, 14]. **a** Temperature dependence of $S(Q, E)$ with incident energy of $E_i = 2.64$ meV taken at AMATERAS, which shows free orientational motion begins at the temperature range 300–320 K. **b** Schematic figure of "orientation-disordered crystal", in which the center of each molecule has a regular crystalline arrangement, but each molecule can rotate freely. **c** Crystal lattice of NPG in the low-temperature phase. The brown, red, and pink spheres represent carbon, oxygen, and hydrogen atoms, respectively. Reproduced with permission from Ref. [13]

peak". In general, glass materials are known to have low-energy harmonic vibrations called boson peaks [15]. Many studies have been conducted to investigate the origin of boson peaks [16], where the material most studied is SiO_2 glass. For a recent example, SiO_2 glass with a new structure in the sense of a high first-sharp diffraction peak has been prepared, and changes in the boson peaks have been reported [17].

In 2021, a "magnetic boson peak" was reported in a spin glass state. To answer the fundamental question of whether there are magnetic excitations inherent in spin glass, Kofu et al. measured magnetic excitations in a magnetic ionic liquid C4mimFeCl$_4$ at a low temperature of 0.3 K in a glassy solid state as well as in a crystalline state [18]. Here, C4mimFeCl$_4$ contains iron as an anion (Fig. 6.6) and takes the liquid state at room temperature. It can take a crystalline or glass solid state, depending on the cooling rate. The sample is deuterated to avoid the strong incoherent scattering from H atoms. As a result of INS, they found a "magnetic boson peak", as shown in Fig.

(a)

1-butyl-3-methylimidazolium
(C4mim)

tetrachloroferrate
(FeCl$_4$)

(b)
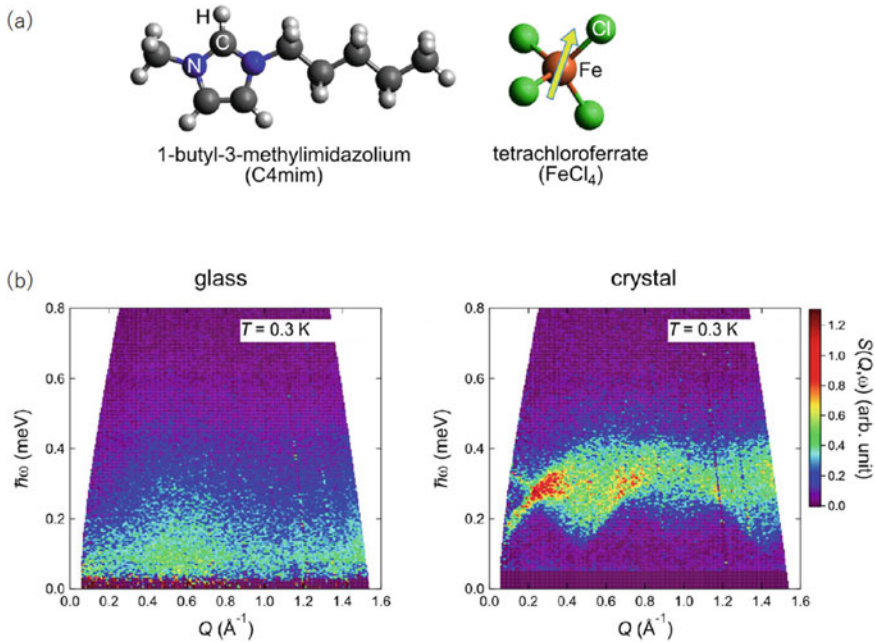
Fig. 6.6 Molecular structure of magnetic ionic liquid C4mimFeCl$_4$ and its magnetic excitations [18]. **a** Molecular structure. The arrow indicates that the FeCl$_4^-$ anion has a spin of 5/2. **b** Magnetic boson peak in the glass state and spin-wave excitations in the crystalline state. Reproduced from Ref. [18]. CC-BY 4.0

6.6, that is considered to be caused by the lack of magnon propagation, reflecting the lack of periodicity. The boson peak observed here is due to magnons and not vibrations.

In 2022, a boson peak seems to have been observed in a material that could be classified as a crystal in a sense [19]. The crystal structure of $Ba_{1-x}Sr_xAl_2O_4$ can be regarded as a network of AlO$_4$ oxygen tetrahedra penetrating into the Ba sublattice formed by the periodic placement of Ba atoms. Ishii et al. found a "sublattice glassy state" in which the periodicity of Ba is maintained and the AlO$_4$ network becomes glassy. Notably, $Ba_{1-x}Sr_xAl_2O_4$, although clearly a crystalline solid, exhibits thermal properties commonly found in amorphous solids, such as low thermal conductivity comparable to that of SiO$_2$ glass. The "sublattice glassy state" can be created by a simple method of uniformly mixing and heating raw materials. In this study, the boson peak played the role of showing the amorphous nature of the sample, where AMATERAS was used for the measurement.

6.5 Inelastic X-Ray Scattering (IXS)

In the 1990s, IXS was put into practical use for investigating the phonon dynamics of materials, owing to the remarkable development of synchrotron radiation facilities and X-ray spectroscopic techniques [20]. The most characteristic feature of this technique is that the incident X-ray energy is on the order of 10 keV, while the phonon excitation energy of interest is on the order of meV. Thus, a resolving power of 10^7 is necessary, which can be achieved by a sharp monochromatic technique using a large synchrotron radiation facility and sophisticated techniques in X-ray optics. Several high-resolution IXS spectrometers are in operation all over the world, i.e., BL35XU [21] and BL43XU [22] at SPring-8, Japan, ID28 [23] at ESRF, France, and sector 3 [24] and 30 [25] at APS, USA. The minimum energy resolution of IXS is 0.84 meV FWHM [26] at present.

IXS measurements have four advantages over INS. First, samples as small as 0.1 mm or less can be measured. In the case of INS, on the other hand, the sample size is typically 1 mm–1 cm. Second, because the incident X-ray energy is very large (about 10 keV), the E and Q are separated, in contrast to Equation 6.2 for neutrons, and the accessible $Q–E$ range is simple, in contrast to that shown in Fig. 6.3 for INS, making it possible to measure phonon excitations of light elements, such as liquid Li, with sound speeds of about 4500 m/s [27].

Third, there is no need to deuterate the sample. This advantage is relevant only if the sample contains hydrogen atoms. For neutrons, the incoherent-scattering cross section of hydrogen atoms is 80 barn [7, 8], which is more than 10 times larger than that of other elements and causes high background. This can be critical because the intensity of inelastic scattering is low compared with that of elastic scattering. Thus deuterium substitution is usually recommended. However, not only can deuterated substitution be difficult and expensive, but there is also concern that it may alter physical properties such as the dispersion relation of phonons. With X-rays, there is no need for deuterium substitution.

Fourth, since synchrotron radiation X-rays are usually horizontally polarized, longitudinal and transverse phonons can be separately observed by selecting appropriate crystal angles with respect to the incident X-rays, as explained later.

The disadvantage of IXS to INS is that light elements are difficult to see because the magnitude of the atomic scattering factors is ordered by atomic number; for atomic scattering factors for X-rays, see Ref. [28, 29].

The energy resolution power of about 10^7 is achieved by a sharp monochromatic technique with a backscattering geometry of Si(9 9 9), Si(11 11 11), or Si(13 13 13). With this technique, energy resolutions of about 3.0 [27], 1.5 [1], and 1.0 meV [26] can be achieved at incident X-ray energies of 17.793, 21.747, and 23.724 keV, respectively.

Figure 6.7 shows a schematic view [30] of a typical IXS spectrometer at BL35XU of SPring-8 [31]. The X-rays generated from an undulator insertion device at a large storage ring are roughly monochromatized by a liquid-N_2-cooled Si(111) double crystal and raised up to obtain sufficient working space again by two Si(111) crys-
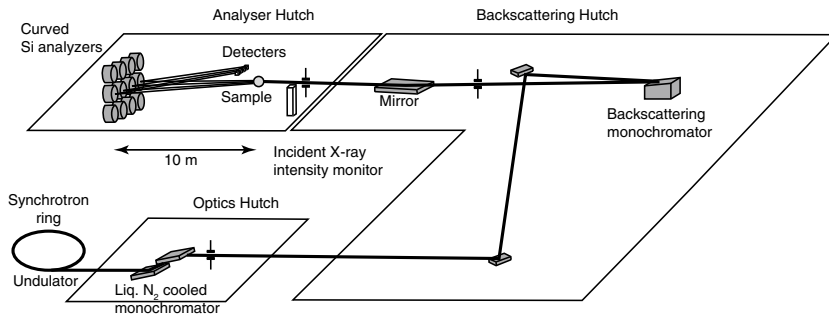
Fig. 6.7 Schematic view of a typical IXS spectrometer. Reproduced with permission from Ref. [30]

tals. The X-ray beam is highly resolved by using a Si(11 11 11) backscattering monochromator with a scattering angle of about 89.98° and focused onto the sample with a bent mirror. The incident beam size is about 0.1×0.1 mm^2. The scattered X-rays travel about 10 m, again are backscattered and focused by 12 Si(11 11 11) curved energy analyzer crystals, travel again about 10 m, and are finally detected near the sample position by 12 CdZnTe detectors.

The energy scan is conducted by changing the temperature of the backscattering monochromator crystal by on the order of 1 K, while the temperatures of the analyzer crystals are kept unchanged within ±1 mK during the experiments. The energy is calibrated by using known phonon energies of a diamond crystal, and the temperature/energy ratio of the monochromator is obtained to be about 18 mK/meV. The energy resolution of the IXS spectrometer was obtained as the elastic peak width of a Plexiglas® sample until very recently, but that of TEMPAX® glass has been found to be more correct. In addition, using the horizontal linear polarization of the incident X-ray beam, longitudinal and transverse phonons can be separately observed by adjusting the crystal angles with respect to the incident beam.

The above descriptions are for general IXS setups, and much smaller sample sizes of μm order (about 4×4 μm^2) where a diamond anvil cell (DAC) is applicable by using a Kirkpatrick–Baez mirror [32], as well as high temperatures up to 3000 K by using a laser heating system, expand investigation targets to those in the geoscience field within the earth.

Here, we introduce recent IXS measurements on typical functional materials from the view point of hyperordered structures science. Mg is a light element, and because this metal is soft, chemically active, and flammable, it was believed that Mg cannot be used as a structural material like Al, although this element can easily be retrieved from the sea. In 2001, however, these disadvantages of Mg were found to be rectified by adding small amounts of Zn and rare-earth metals [33]. Because of the excellent properties together with the ease of recycling, the Mg alloys are expected to be next-generation structural materials for bodies of subway trains or even aircraft, for example.
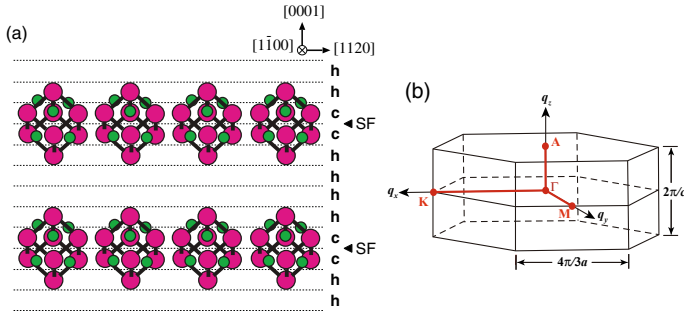
Fig. 6.8 **a** Schematic of Zn_6Y_8 clusters in long-period stacking ordered (LPSO) phase located at stacking faults. **b** First Brillouin zone of *hcp* structure of pure Mg. Reproduced with permission from Ref. [35]

The origin of the remarkable properties was clarified by a scanning transmission electron microscopy (STEM) technique with an atomic-resolution angle annular dark-field (HAAF) function. The formation of clusters of Zn_6Y_8 fragments of *fcc* structure embedded in a long-period stacking ordered (LPSO) phase was found to play an important role (see Fig. 6.8a) [34].

To clarify the impurity effects in the microscopic elastic properties of the revolutionary Mg alloys, IXS experiments were carried out on a $Mg_{85}Zn_6Y_9$ crystal at room temperature at BL35XU of SPring-8 [35, 36]. Figure 6.9 shows logarithmic plots of the IXS spectra of an $Mg_{85}Zn_6Y_9$ single crystal for the (a) longitudinal and (b) transverse modes along the Γ-A direction. The first Brillouin zone of a *hcp* structure of pure Mg is given in Fig. 6.8b, and the Γ-A direction is along the *c*-axis. In (a) and (b), several excitation modes are observed in the Brillouin zone. Among them, two types are seen, one showing clear dispersion relations with Q, as indicated by arrows and the other having no dispersion, i.e., localized modes, given by dashed lines.

Figure 6.9c shows the dispersion curves along the Γ-A direction, in which circles and triangles represent the longitudinal and transverse modes, and closed and open marks denote clear peaks and broad shoulders, respectively. The dispersive excitations are mostly located on those of pure Mg given by solid curves. Additionally, dispersion-less excitations are newly observed at about 4, 10, and 17 meV, as shown by the dashed lines. Exactly the same dispersion relations are observed in the Γ-K and Γ-M directions, perpendicular to the *c*-axis [35]. An ab initio molecular dynamics simulation was carried out to obtain the vibrational density of states (DOS) for this system. The 4, 10, and 17 meV modes are interpreted as the twisting and stretching modes and between the cluster and host Mg atoms. As another example of phonon dispersion measurements of heavy-element-doped inorganic materials, Kimura et al. reported on Ta-doped Fe_2VAl Heusler-type thermoelectric materials [37].

Another study that has yielded important results at BL35XU is the measurement of the dispersion relation of rubrene ($C_{42}H_{28}$), a well-studied high-mobility organic semiconductor [38]. This result is important because phonons are considered to play a major role in the physical properties of molecular solids [39]. The mechanism
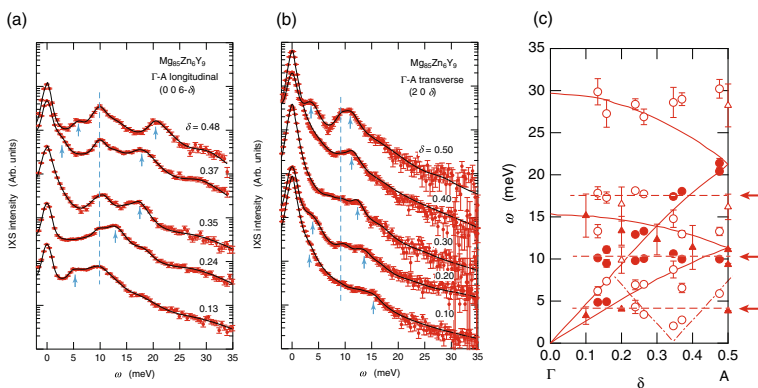
Fig. 6.9 Logarithmic plots of IXS spectra of $Mg_{85}Zn_6Y_9$ single crystal for **a** longitudinal and **b** transverse modes, and **c** dispersion relation of longitudinal (circles) and transverse (triangles) excitations along the Γ-A direction. The solid curves in **c** represent the dispersion relation of pure Mg. Reproduced with permission from Ref. [35]

of electrical conduction in high-mobility organic semiconductors differs from that of the general band conduction in inorganic semiconductors such as Si, and it is currently believed that the behaviors of phonons inevitably explain it. Nevertheless, phonons in organic molecular crystals generally have more than 100 branches, and even with neutron scattering, there have been few measurements of dispersion relations in organic semiconductors [40]. Since phonons are considered to be strongly involved in the electrical conduction of high-mobility organic semiconductors [41], this research is important to the study of materials such as those of organic electroluminescence displays. Moreover, it is known to be difficult to reproduce weak forces such as intermolecular forces in first-principles calculations, and the measurement of dispersion relations will be useful to verify such forces. Note that it is becoming possible to measure phonon dispersions of nondeuterated single crystals with a size of 1 mm^3 or smaller because one must deuterate the samples to reduce the background level when the measuring method is INS, and also the sample size must be larger for INS. The successful measurement of the dispersion relation of rubrenes is thus a significant development.

6.6 Nuclear Resonant Inelastic X-Ray Scattering (NRIXS)

NRIXS is a method by which we can selectively measure $S(Q, E)$ of atoms that have Mössbauer nuclei that can be excited by synchrotron radiation. Figure 6.10a shows a schematic view of a typical NRIXS setup [42]. The X-rays generated from an undulator insertion device are roughly monochromatized by a Si or diamond double crystal and highly resolved by several types of high-resolution monochromator, such
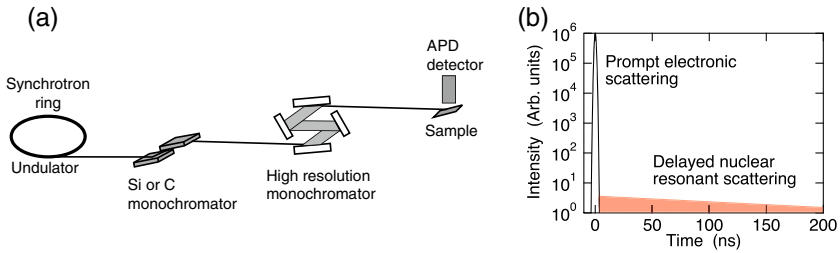
Fig. 6.10 **a** Schematic of a typical NRIXS spectrometer and **b** typical NRIXS signal with time. The figures are drawn with reference to Ref. [44]

as dispersive channel-cut or nested configuration monochromators, depending on the outgoing X-ray energy and resolution of the target element [43]. The intensity of the incident beam is usually monitored with an ionization chamber. The well-resolved X-rays are irradiated onto the sample including an appropriate isotope, and the emitted X-rays are detected with an avalanche photodiode (APD) detector with a time resolution of 1 ns order.

Figure 6.10b shows a typical time response of the signal, which is composed of a prompt peak scattered by electrons in the sample and a long-lasting delayed NRIXS signal [44]. Thus, pulsed synchrotron X-rays with a pulse interval of about 100 ns are essential for observing the phonon DOS of the sample. Similar to the nonresonant IXS experiments, NRIXS measurements under high temperatures and pressures are possible by using DAC with laser heating [45].

Atomic dynamics of impurity atoms in a simple metal are one of the key issues concerning hyperordered structure of materials. Seto et al. [44] measured NRIXS spectra of the ^{57}Fe isotope in highly diluted (0.017 and 0.1 at.%) Fe in Al and Cu metals, respectively, to investigate the local vibrational DOSs of Fe impurities. The measurements were carried out at room temperature at BL09XU of SPring-8. The storage ring was operated in a special timing mode having a bunch interval of 228 ns. A bandwidth of 3.2 meV full-width at half-maximum for the incident X-ray beam was obtained by using a nested high-resolution monochromator consisting of asymmetric Si(511) and asymmetric (975) channel-cut crystals. The energy of the radiation was scanned around the nuclear resonant energy of ^{57}Fe of 14.413 keV.

Figure 6.11 shows the NRIXS spectra of ^{57}Fe in (a) Al and (b) Cu metals. In both spectra, peaks are observed at the excitation energy of about 14 meV. Another peak is seen in (b) at about 30 meV, while the spectrum in (a) shows only a small tail in this energy range. A theoretical calculation was performed for investigating these special features in the NRIXS spectra, and it was found that the 14 meV peaks originate from the resonance with the vibrational modes of the host Al atoms, while the 30 meV peak is interpreted as a localized mode of the impurity Fe atoms.
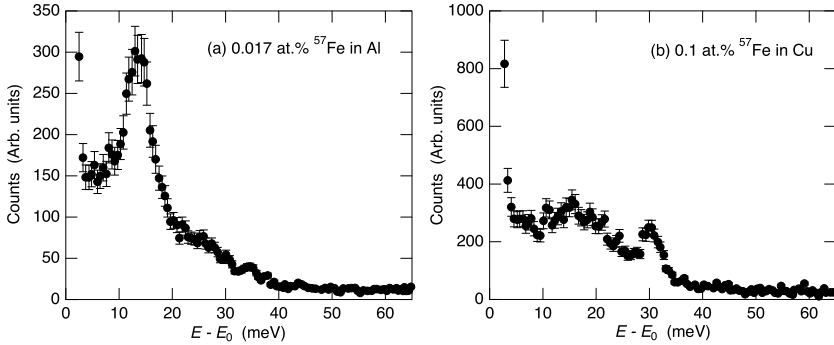
Fig. 6.11 NRIXS spectra of diluted ^{57}Fe in **a** Al and **b** Cu metals. Reproduced with permission from Ref. [44]

6.7 Time-Domain Interferometry (TDI)

The Mössbauer effect is an extremely sharp resonance effect. For example, the gamma rays elastically emitted from ^{57}Fe excited nuclei, as also described in Sect. 6.6, provide very good monochromatic light with an energy width of $\Gamma_0 = 4.7$ neV, which could be an ideal incident light for dynamics measurements with neV resolution. The arrangement shown in Fig. 6.12 is used to measure $I(Q, t)$ for general materials that do not contain Mössbauer nuclides.

In general interferometry, light is interfered through different paths in space by splitting the light with a half-mirror and stacking them again. In this method, however, as shown in Fig. 6.12c, the light is interfered through different paths in time, which is called time-domain interferometry (TDI) [46]. The most basic TDI concept can be understood as follows [47]. Assume that there is no sample in the TDI in Fig. 6.12 and a scattering angle 2θ of zero [48]. The excitation of ^{57}Fe nuclei by synchrotron radiation produces strongly forward-directed Mössbauer gamma rays at Fe-1 in Fig. 6.12. If the energy of the gamma rays emitted from another ^{57}Fe (Fe-2 in Fig. 6.12) is shifted by the Doppler effect, for example, the interference between the gamma rays from Fe-1 and Fe-2 will produce a beat that can be observed. An avalanche photodiode (APD) is used for the detector, as described in Sect. 6.6. If the sample to be measured is placed between Fe-1 and Fe-2, and the detector is placed in the direction of 2θ after the momentum transfer with the sample, the light passing through path-1 and path-2 in Fig. 6.12 will be scattered by the sample at different times. Therefore, the intermediate scattering function $I(Q, t)$ (Eq. 6.1) of the sample can be measured as the amplitude of the interference pattern. However, it was shown that the correct $I(Q, t)$ cannot be obtained by simply using TDI with a single gamma-ray wavelength because of the finite energy width of the incident light. In practice, therefore, "multiline" TDI was performed to obtain the correct $I(Q, t)$ by applying a magnetic field to Fe-1 and Fe-2 to exploit the hyperfine structure of the nuclear
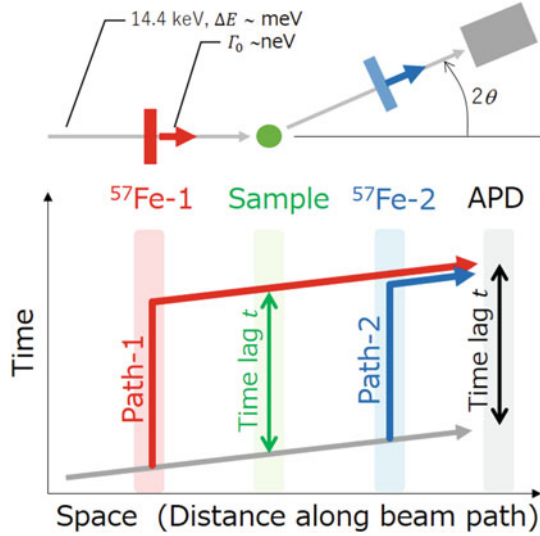
energy levels and using monochromatic gamma rays of several different energies [49].

The momentum (space)–energy (time) regions covered by TDI are shown in Fig. 6.1, from which one can see that it covers areas that could not be measured previously. Here, we introduce the following discovery due to the ability of measurement in spatial and temporal domains that were previously unmeasurable.

Figure 6.13 shows the inverse temperature dependence of the relaxation time $\langle \tau \rangle$ of supercooled o-terphenyl measured by TDI [50]. Here, o-terphenyl is a typical glass-forming material that has been intensively studied. In the supercooled liquid state of glass-forming materials, a subnanometer-scale relaxation process called Johari–Goldstein (JG) relaxation can be observed at temperatures below the melting point T_m as shown in Fig. 6.13a, but the space scale of the branching of JG relaxation from the α relaxation, i.e., diffusion, had been unknown because of the lack of a measurement technique that covers the space and time range simultaneously.

Figure 6.13b shows that there is no branching of JG relaxation in the main peak region of $S(Q)$. This means that the branching of JG relaxation does not occur at the scale of intermolecular size. However, a crossover from the $1/T$-dependence of the JG relaxation from the slope of α relaxation is observed in the larger Q region, i.e., on a more localized space scale. This is the first experimental result of observing the branching of the JG relaxation and clarifying its origin from a microscopic viewpoint in molecular glasses.

TDI uses meV-resolution synchrotron radiation pulses to excite ^{57}Fe nuclei and is currently available at BL35XU in SPring-8, Japan.
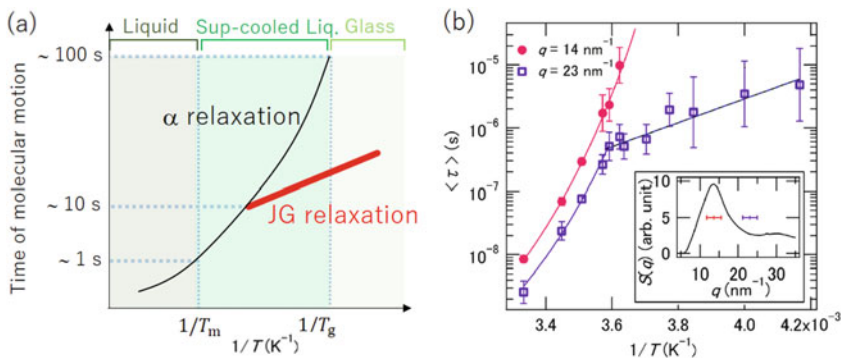
Fig. 6.13 Inverse temperature dependence of molecular motion time related to glass transition. **a** General conceptual picture of the glass transition of liquids. Sup-cooled Liq. denotes supercooled liquid. **b** TDI measurement results of the relaxation time $\langle \tau \rangle$ for *o*-terphenyl. The inset shows the $S(Q)$ and Q regions of TDI measurements. Reproduced with permission from Ref. [50]

6.8 Summary and Perspective

In this article, we review the remarkable experimental developments in the methods for observing the dynamics of materials using quantum beams of X-rays and neutrons from recently improved sources, e.g., SPring-8 and J-PARC, respectively. Functional materials having the so-called hyperordered structure usually include a hidden atomic configuration that cannot be easily clarified by experimental studies for static and averaged atomic structures. It is well known that traditional dynamic methods of Raman scattering and IR spectroscopy yield useful and additional information about local atomic arrangements of molecules and covalent materials, indicating that dynamic experiments reveal hidden information of materials. Nowadays, we can evaluate many dynamic properties by using improved quantum beams, as introduced in this article. Therefore, it is, at present, very important for scientists to know a wide range of both the properties of a researched material caused by an expected hyperordered structure and the advantages/disadvantages of the experimental methods for investigating the dynamics of materials. We expect that readers will gain new insights for investigating the science of materials by considering the dynamic properties when handling functional materials.

References

1. Monaco G (2008) C R Phys 9:608
2. Van Hove L (1954) Phys Rev 95:249
3. See §7 in Sakurai JJ (1994) Modern quantum mechanics, revised edn. In: Tuan SF (ed). Addison-Wesley
4. Brockhouse BN (1959) Phys Rev Lett 2:287
5. https://mlfinfo.jp/en/bl02/. Accessed 10 Dec 2022
6. Shirane G, Minkiewicz VJ, Nathans R (1968) J Appl Phys 39:383
7. Dianoux A-J, Lander G (2003) Neutron data booklet, 2nd edn. OCP Science, Philadelphia
8. https://www.ncnr.nist.gov/resources/n-lengths/. Accessed 10 Dec 2022
9. Lovesay SW (1984) Theory of neutron scattering from condensed matter. Oxford University Press, Oxford
10. Bee M (1988) Quasielastic neutron scattering. Adam-Hilger, Bristol and Philadelphia
11. Nakajima K, Ohira-Kawamura S, Nakamura M, Kajimoto R, Inamura Y, Takahashi N, Aizawa K, Suzuya K, Shibata K, Nakatani T, Soyama K, Maruyama R, Tanaka H, Kambara W, Iwahashi T, Itoh Y, Osakabe T, Wakimoto S, Kakurai K, Maekawa F, Harada M, Oikawa K, Lechner RE, Mezei F, Arai M (2011) J Phys Soc Jpn 80:SB028
12. https://mlfinfo.jp/en/bl14/. Accessed 10 Dec 2022
13. Li B, Kawakita Y, Ohira-Kawamura S, Sugahara T, Wang H, Wang J, Chen Y, Kawaguchi SI, Kawaguchi S, Ohara K, Li K, Yu D, Mole R, Hattori T, Kikuchi T, Yano S, Zhang Z, Zhang Z, Ren W, Lin S, Sakata O, Nakajima K, Zhang Z (2019) Nature 567:506
14. https://www.jaea.go.jp/02/press2018/p19032902/ (in Japanese). Accessed 2 Feb 2022
15. Krishnan RS (1953) Proc Indian Acad Sci A 37:377
16. For review, Nakayama T (2002) Rep Prog Phys 65:1195
17. Onodera Y, Kohara S, Salmon PS, Hirata A, Nishiyama N, Kitani S, Zeidler A, Shiga M, Masuno A, Inoue H, Tahara S, Polidori A, Fischer HE, Mori T, Kojima S, Kawaji H, Kolesnikov AI, Stone MB, Tucker MG, McDonnell MT, Hannon AC, Hiraoka Y, Obayashi I, Nakamura T, Akola J, Fujii Y, Ohara K, Taniguchi T, Sakata O (2020) NPG Asia Mater 12:85
18. Kofu M, Watanuki R, Sakakibara T, Ohira-Kawamura S, Nakajima K, Matsuura M, Ueki T, Akutsu K, Yamamuro O (2021) Sci Rep 11:12098
19. Ishii Y, Yamamoto A, Sato N, Nambu Y, Ohira-Kawamura S, Murai N, Ohara K, Kawaguchi S, Mori T, Mori S (2022) Phys Rev B 106:134111
20. Burkel E (2000) Rep Prog Phys 63:171
21. http://www.spring8.or.jp/wkg/BL35XU/instrument/lang/INS-0000000515/instrument_summary_view. Accessed 10 Dec 2022
22. http://user.spring8.or.jp/sp8info/?p=3138. Accessed 10 Dec 2022
23. https://www.esrf.fr/home/UsersAndScience/Experiments/EMD/ID28.html. Accessed 10 Dec 2022
24. https://www.aps.anl.gov/Beamlines/Directory/Details?beamline_id=6. Accessed 10 Dec 2022
25. https://www.aps.anl.gov/Sector-30/IXS-Technique. Accessed 10 Dec 2022
26. Ishikawa D, Baron AQR (2021) J Phys Soc Jpn 90:083602
27. Scopigno T, Balucani U, Ruocco G, Sette F (2000) J Phys: Condens Matter 12:8009
28. Prince E (ed) (2006) International tables for crystallography, vol C, Mathematical, physical and chemical tables. Wiley/Int'l Union for Crystallography
29. https://it.iucr.org//Cb/. Accessed 10 Dec 2022
30. Hosokawa S, Inui M, Kajihara Y, Tsutsui S, Baron AQR (2015) J Phys: Condens Matter 27:194104
31. Baron AQR, Tanaka Y, Goto S, Takeshita K, Matsushita T, Ishikawa T (2000) J Phys Chem Solids 61:461–465
32. Baron AQR, Ishikawa D, Fukui H, Nakajima Y (2019) AIP Conf Proc 2054:020002
33. Kawamura Y, Hayashi K, Inoue A, Masumoto T (2001) Mater Trans 42:1172
34. Abe E, Ono A, Itoi T, Yamasaki M, Kawamura Y (2011) Phil Mag Lett 91:690

35. Hosokawa S, Kimura K, Stellhorn JR, Yoshida K, Hagihara K, Izuno H, Yamasaki M, Kawamura Y, Mine Y, Takashima K, Uchiyama H, Tsutsui S, Koura A, Shimojo F (2018) Acta Mater 146:273
36. Hosokawa S, Kimura K, Yamasaki M, Kawamura Y, Yoshida K, Inui M, Tsutsui S, Baron AQR, Kawakita Y, Itoh S (2017) J Alloys Compd 695:426
37. Kimura K, Yamamoto K, Hayashi K, Tsutsui S, Happo N, Yamazoe S, Miyazaki H, Nakagami S, Stellhorn JR, Hosokawa S, Matsushita T, Tajiri H, Ang AKR, Nishino Y (2020) Phys Rev B 101:024302
38. Takada K, Yoshimi K, Tsutsui S, Kimura K, Hayashi K, Hamada I, Yanagisawa S, Kasuya N, Watanabe S, Takeya J, Wakabayashi Y (2022) Phys Rev B 105:205205
39. Fratini S, Nikolka M, Salleo A, Schweicher G, Sirringhaus H (2020) Nat Mater 19:491
40. For example, see Natkaniec I, Bokhenkov EL, Dorner B, Kalus J, Mackenzie GA, Pawley GS, Schmelzers U, Sheka EF (1980) J Phys C: Solid St Phys 13:4265
41. Coropceanu V, Cornil J, da Silva Filho DA, Olivier Y, Silbey R, Brédas J-L (2007) Chem Rev 107:926
42. Seto M, Yoda Y, Kikuta S, Zhang XW, Ando M (1995) Phys Rev Lett 74:3828
43. Alp EE, Sturhahn W, Toellner TS, Zhao J, Hu M, Brown DE (2002) 144/145:3
44. Seto M, Kobayashi Y, Kitao S, Haruki R, Mitsui T, Yoda Y, Nasu S, Kikuta S (2000) Phys Rev B 61:11420
45. Lin J-F, Sturhahn W, Zhao J, Shen G, Mao H-K, Hemley RJ (2005) In: Chen J, Wang Y, Duffy TS, Shen G, Dobrzhinetskaya LP (eds) Advances in high-pressure techniques for geophysical applications. Elsevier, Amsterdam, p 397
46. Baron AQR, Franz H, Meyer A, Rüffer R, Chumakov AI, Burkel E, Petry W (1997) Phys Rev Lett 79:2823
47. Smirnov GV, van Bürck U, Arthur J, Popov SL, Baron AQR, Chumakov AI, Ruby SL, Potzel W, Brown GS (1996) Phys Rev Lett 77:183
48. Saito M, Yamaguchi T, Nagao M (2022) Butsuri 77:690 (in Japanese)
49. Saito M, Masuda R, Yoda Y, Seto M (2017) Sci Rep 7:12558
50. Saito M, Kitao S, Kobayashi Y, Kurokuzu M, Yoda Y, Seto M (2012) Phys Rev Lett 109:115705